



Cite as
Nano-Micro Lett.
(2023) 15:126

Received: 6 March 2023
Accepted: 6 April 2023
© The Author(s) 2023

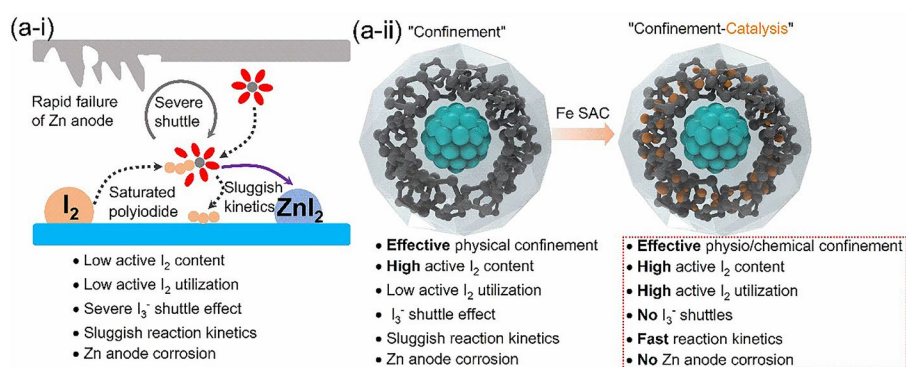
Aqueous Zinc Batteries with Ultra-Fast Redox Kinetics and High Iodine Utilization Enabled by Iron Single Atom Catalysts

Xueya Yang¹, Huiqing Fan¹ ✉, Fulong Hu², Shengmei Chen³, Kang Yan¹, Longtao Ma² ✉

HIGHLIGHTS

- The porous structure and interconnected conductive pathways accommodate a large amount of iodine, entrap polyiodides and guarantee its efficient utilization. While the Fe single atom catalyst efficiently catalyzes the iodine/polyiodide conversion.
- With “confinement-catalysis” host, the Zn||I₂ battery delivers a high capacity of 188.2 mAh g⁻¹ at 0.3 A g⁻¹, excellent rate capability with a capacity of 139.6 mAh g⁻¹ at 15 A g⁻¹ and ultra-long cyclic stability over 50,000 cycles with 80.5% initial capacity retained under high iodine loading of 76.72 wt%.

ABSTRACT Rechargeable aqueous zinc iodine (Zn||I₂) batteries have been promising energy storage technologies due to low-cost position and constitutional safety of zinc anode, iodine cathode and aqueous electrolytes. Whereas, on one hand, the low-fraction utilization of electrochemically inert host causes severe shuttle of soluble polyiodides, deficient iodine utilization and sluggish reaction kinetics. On the other hand, the usage of high mass



polar electrocatalysts occupies mass and volume of electrode materials and sacrifices device-level energy density. Here, we propose a “confinement-catalysis” host composed of Fe single atom catalyst embedding inside ordered mesoporous carbon host, which can effectively confine and catalytically convert I₂/I⁻ couple and polyiodide intermediates. Consequently, the cathode enables the high capacity of 188.2 mAh g⁻¹ at 0.3 A g⁻¹, excellent rate capability with a capacity of 139.6 mAh g⁻¹ delivered at high current density of 15 A g⁻¹ and ultra-long cyclic stability over 50,000 cycles with 80.5% initial capacity retained under high iodine loading of 76.72 wt%. Furthermore, the electrocatalytic host can also accelerate the I⁻ ↔ I₂ conversion. The greatly improved electrochemical performance originates from the modulation of physicochemical confinement and the decrease of energy barrier for reversible I⁻/I₂ and I₂/I⁺ couples, and polyiodide intermediates conversions.

KEYWORDS Aqueous zinc batteries; Iodine reduction reaction; Fe single atom catalysts

✉ Huiqing Fan, hqfan3@163.com; Longtao Ma, iamltma@nwpu.edu.cn

¹ State Key Laboratory of Solidification Processing, School of Materials Science and Engineering, Northwestern Polytechnical University, Xi'an 710072, People's Republic of China

² Frontiers Science Center for Flexible Electronics, Institute of Flexible Electronics, Northwestern Polytechnical University, Xi'an 710072, People's Republic of China

³ Department of Materials Science and Engineering, City University of Hong Kong, 83 Tat Chee Avenue, Kowloon 999077, Hong Kong, People's Republic of China

Published online: 20 May 2023



SHANGHAI JIAO TONG UNIVERSITY PRESS

Springer

1 Introduction

Rechargeable aqueous zinc-iodine ($\text{Zn}||\text{I}_2$) batteries based on elemental iodine/iodide ion conversion is regarded as promising energy storage technologies in consideration of their admissible energy density, immanent safety, cost position, Earth abundance and environmental friendliness [1–8]. Nevertheless, the intrinsically poor electrical conductivity of iodine and the dissolution of iodine/polyiodide intermediates account for grossly underutilized active iodine and severely detrimental shuttle effects, causing low actual capacity delivered, deficient reaction kinetics, fast capacity fading, short lifespan and metal anode corrosion [9–15]. The common tactics are to infuse iodine into diversified inert porous carbon nanostructures through the physical adsorption, which establishes inactive electronic transmission pathway with the active iodine encapsulated and ensnares soluble polyiodide intermediates. Although this sole confinement strategy can partially alleviate above issues employing low fraction of the electrochemically inert host material in the electrode, the reversibility of iodine conversion, active iodine utilization and reaction kinetics are still far from the application demand of high energy density, high power density and long cyclic stability especially under high iodine loading (> 60 wt%) and in thick iodine electrode configuration [16, 17].

To address the reversibility, utilization and kinetic issues of the iodine cathode, iodine/polyiodide electrocatalysis is designed to reduce activation energy barriers for fast kinetics and efficient iodine conversion, which is reflected in reduced polarization, fast rate response and extended cycling lifespan on battery performance. The desired electrocatalysts for boosting iodine/polyiodide conversion emphasize these features: (1) excellent electrical conductivity facilitating electron/ion transportation; (2) favorable physio-/chemisorption stabilizing iodine/polyiodide; (3) competently electrocatalytic capability accelerating the iodine/polyiodide conversions. To date, various polar materials such as metal oxides, metal nitrides, metal phosphide and metal organic frameworks are reported as polarized hosts for $\text{Zn}||\text{I}_2$ batteries [18–22]. Despite the rate capability and cyclic stability is remarkably enhanced with electrocatalytic hosts, the weight percentage of inactive components are tremendously increased in the whole electrode, leading to relatively low actual iodine loading (< 60 wt%). The low iodine loading will significantly comprise the practical volumetric/

gravimetric energy density of $\text{Zn}||\text{I}_2$ batteries in real device [23, 24]. It is difficult to exploit a simplex host material that can simultaneously satisfy efficient confinement and favorable electrocatalysis.

In this work, we propose a “confinement-catalysis” strategy to enable a high iodine loading $\text{Zn}||\text{I}_2$ battery with fast reaction kinetics and ultra-long cycling stability by embedding iron single atom catalyst (SAC) in ordered mesoporous conductive framework as a catalytic iodine host. With this design, the porous structure and interconnected conductive pathways accommodate a large amount of iodine, entrap polyiodides and guarantee its efficient utilization. While the Fe SAC efficiently catalyzes the iodine/polyiodide conversion. Considering the synergistic contribution of high catalytic and iodine/polyiodide adsorption ability from host framework, the $\text{Zn}||\text{I}_2$ battery achieves ultra-high-rate capability at 15 A g^{-1} with a capacity of 139.6 mAh g^{-1} delivered and ultra-long cycling stability over 50,000 cycles with 80.5% initial capacity retained at 5 A g^{-1} under 76.72 wt% iodine loading condition. This work opens a way to shortens the gap between research and application for $\text{Zn}||\text{I}_2$ batteries.

2 Results and Discussion

2.1 Formulation of Fe Single Atom Catalyst-based Host

With the traditional disordered activated carbon (AC) as insulating active iodine (I_2) host, although the electrode achieves good electrical conductivity, the sluggish reaction kinetics, low active I_2 content, low active I_2 utilization and severe shuttle effects become the bottleneck to realize stably high energy $\text{Zn}||\text{I}_2$ batteries (Fig. 1a-i). The mesoporous carbon with abundant pores and ordered pores structure can physically confine active I_2 , generated I_3^- intermediates and finally ZnI_2 , increasing the active I_2 content and partially alleviating I_3^- shuttle effect (Fig. 1a-ii). Nonetheless, poor redox kinetics has always been the intrinsic difficulty for the iodine redox reactions that proceed at multiphase boundaries. The electrocatalyst is essential to reduce active I_2 conversion energy barriers (Fig. 1a-iii) and accelerate the iodine redox reactions. For I_2/I_3^- electrocatalysts, its mass proportion should be kept to a minimum for overall high energy density. The single atom catalyst (SAC) with activated and isolated catalytic metal atoms presents the best catalytic sites utilizations for catalytic reactions. In this

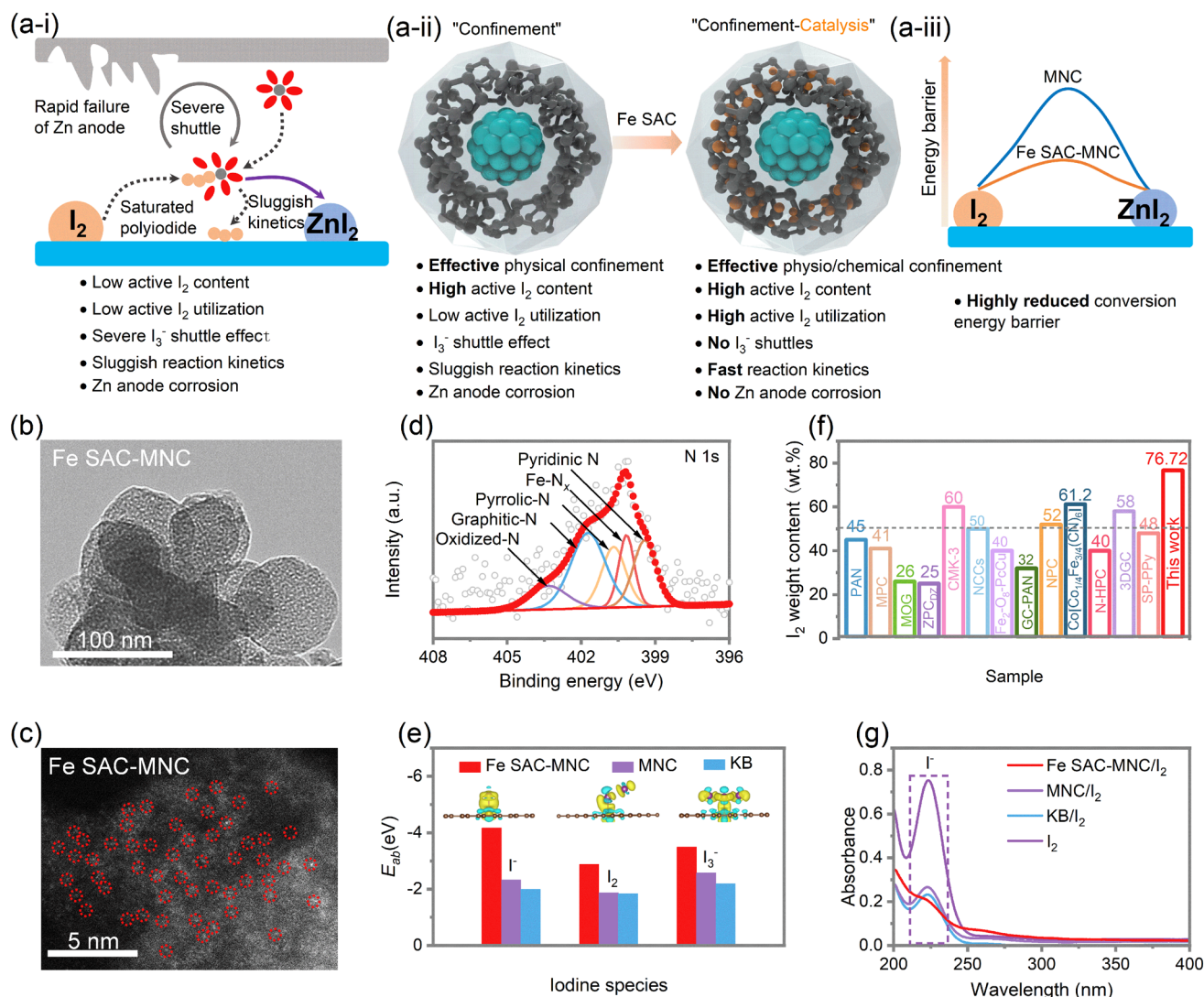


Fig. 1 **a-i** Schematic illustration of iodine redox reaction in aqueous Zn||I₂ batteries. **a-ii** Design strategy of “confinement-catalysis” for high-performance iodine cathode. **a-iii** Schematic illustration of reduced conversion energy barrier with Fe SAC embedded. **b** TEM images of Fe SAC-MNC. **c** Aberration-corrected HAADF-STEM image of Fe SAC-MNC. **d** High-resolution N 1s XPS spectrum for Fe SAC-MNC. **e** Calculated adsorption energy of I⁻/I₂/I₃⁻ species with Fe SAC-MNC, MNC and KB. Inset: optimized charge-density-difference patterns of I⁻, I₂, and I₃⁻ on Fe SAC-MNC. **f** I₂ weight content of this work compared to the previously reported various hosts in metal-iodine batteries from TGA [29–41]. **g** UV-vis absorption spectra of I₂ in the solution of Fe SAC-MNC/I₂, MNC/I₂ and KB/I₂ adding with 2 M ZnSO₄ (the solution of I₂ adding with 2 M ZnSO₄ as contrast)

work, the Fe SAC on mesoporous nitrogen doped carbon (Fe SAC-MNC) is designed as active I₂ host for aqueous Zn||I₂ batteries. The ordered porous structure can effectively restrain I₂/I₃⁻/ZnI₂, while the Fe SAC significantly reduces the activation energy barrier for outstanding I₂ reduction reaction (IRR) and boosts electrochemical I₂/I₃⁻/ZnI₂ redox kinetics. Owing to this peculiarity, Zn||I₂ batteries display high active I₂ utilization, stable cycle, high coulombic efficiency and high energy density.

Fe SAC-MNC host is prepared by thermal pyrolysis of nanoemulsion-directed UiO-66-NH₂. After pyrolysis, MNC and Fe SAC-MNC exhibit two broad peaks in the 2θ range of 24° and 44°, corresponding to graphitized carbon for (002) and (101) reflections (Fig. S1). In the Raman spectra, the ratio of D peak to G peak reveals the change of material structure to an extent. I_D/I_G ratio of Fe SAC-MNC (0.94) is close to MNC (0.95), declaring that the graphitization extent is not influenced by the introduction of Fe SAC (Fig.

S2). The uniform nanospheres with diameter of ~80 nm and bestrewn abundant ordered mesoporous are depicted by the transmission electron microscopy (TEM, Fig. 1b). The abundant and uniform Fe SAC scattering on MNC is examined by high-angle annular dark-field scanning transmission electron microscopy (HAADF-STEM, Fig. 1c), which is labeled by red cycles for better clarity. X-ray photoelectron spectroscopy (XPS) confirms the interaction between Fe SAC and MNC (Fig. 1d). The high resolution of N 1s XPS spectrum for Fe SAC-MNC is divided into five peaks, corresponding to Pyridinic N (399.4 eV), Fe-N_x (400.2 eV), Pyrrolic-N (400.7 eV), Graphitic-N (401.7 eV) and Oxidized-N (403.3 eV). The characteristic peaks of Fe 2p appeared at 712.25 eV (Fe 2p_{3/2}) and 723.75 eV (Fe 2p_{1/2}), confirming that the oxide state of Fe SAC is +3 (Fig. S3) [25, 26]. To prepare the Fe SAC-MNC/I₂ cathode (MNC/I₂ and KB/I₂ as control groups), the I₂ molecules are successfully confined in the hosts via thermal melt-diffusion routes under high temperature of 120 °C. The successful confinement of I₂ in Fe-SAC-MNC is confirmed by XRD pattern, N₂ adsorption/desorption isotherms and pore size distribution, in which the specific surface area is sharply decreased from 257.9 to 1.84 m² g⁻¹ and the content of pores is remarkably reduced with introduction of I₂ molecules (Figs. S1 and S4) [27]. And TG result shows the slight weight loss in 50 °C. Being considered to the adsorbed water on the surface of the hosts.

In order to investigate thoroughly the deep affinity relation between iodine species and Fe SAC-MNC, referred to MNC and KB, the first-principles density-functional theory (DFT) calculation is performed to describe the interaction of the hosts of Fe SAC-MNC, MNC and KB with I⁻/I₂/I₃⁻ species, supporting exact insight into restraining the shuttle effect. Compared with MNC and KB, the Fe SAC-MNC host exhibits the stronger physical and chemical absorption for all of I⁻/I₂/I₃⁻ species (Fig. 1e). The better confinement of MNC for I⁻, I₂ and I₃⁻ species than that of KB is attributed to ordered pore structure (Fig. S5) [28]. The theoretical results of E_{ab} are listed specifically in Table S1. The optimized charge-density-difference of I⁻, I₂, and I₃⁻ on Fe SAC-MNC, MNC and KB is displayed in inset of Figs. 1e and S5 by colored isosurfaces to describe the electron accumulation (yellow) and depletion (blue). The obvious charge transfer can be observed, and further reveal that the forceful electrostatic interactions between Fe SAC-MNC with I⁻, I₂, and I₃⁻. In light of abundant pore structure for physical confinement and strong chemical affinity, I₂ molecules loading

content in the Fe SAC-MNC/I₂ and MNC/I₂ can reach to high mass ratio of 76.72 and 77.82 wt%, respectively, higher than KB/I₂ (63.35 wt%), which are evaluated by thermogravimetric analysis (TGA, Fig. S6). Notably, comparing with the I₂ weight content in various hosts as cathode of metal-iodine batteries reported previously, Fe SAC-MNC shows an outstanding competitive superiority in the iodine content for 76.72 wt% (Fig. 1f) [29–41].

The ultraviolet–visible (UV–vis) is employed to explore the dissolution of iodine from the Fe SAC-MNC/I₂, MNC/I₂ and KB/I₂ cathodes in the 2 M aqueous ZnSO₄ electrolyte (Fig. 1g). The peaks at 226 nm are indexed to I⁻ species. In contrast to the MNC/I₂ and KB/I₂ cathode, the Fe SAC-MNC/I₂ cathode exhibits lowest peak intensity and the weakest yellow color after 48 h (Fig. S7), demonstrating robust physio/chemisorption of Fe SAC-MNC host to I₂.

2.2 Fast I₂ Reduction Reaction Enabled by Fe SAC Electrocatalysts

For investigating the effect of Fe SAC for electrocatalytic redox conversion of I₂/I⁻, cyclic voltammetry (CV) and electrochemical impedance spectra (EIS) tests are measured in two-electrode configuration with Zn metal as counter electrode and reference electrode, catalyst deposited carbon fiber cloth (CFC) as working electrode and 2 M ZnSO₄ + 0.02 M I₂ aqueous solution as electrolyte [36, 42, 43]. In comparison with MNC (1.35 V; 0.33 mA cm⁻²) and KB (1.29 V; 0.28 mA cm⁻²), the Fe SAC-MNC electrocatalyst exhibit high optimal reduction potential of 1.36 V (vs. Zn/Zn²⁺) and reduction current density of 0.44 mA cm⁻² (Fig. 2a, b), showing the I₂ reduction reaction (IRR) curves of Fe SAC-MNC, MNC or KB as working electrode. Meanwhile, the Fe SAC-MNC electrocatalyst presents smaller Tafel slope (η) of 59.07 mV dec⁻¹, than that of MNC (86.39 mV dec⁻¹) and KB (108.52 mV dec⁻¹) (Fig. 2c). The above results manifest the fast reaction kinetics of I₂/I⁻ redox conversion. To further examine the outstanding IRR activity of Fe SAC-MNC, the EIS measurements are performed at reduction onset potential to monitor charge transfer resistance (R_{ct}). The Fe SAC-MNC electrocatalyst shows smaller R_{ct} (54.47 Ω) (Fig. S8a) and lower slope of Arrhenius curves (Fig. S8b), compared with MNC (145.9 Ω) and KB (90.73 Ω). According to oxygen reduction reaction (ORR), the lower slope

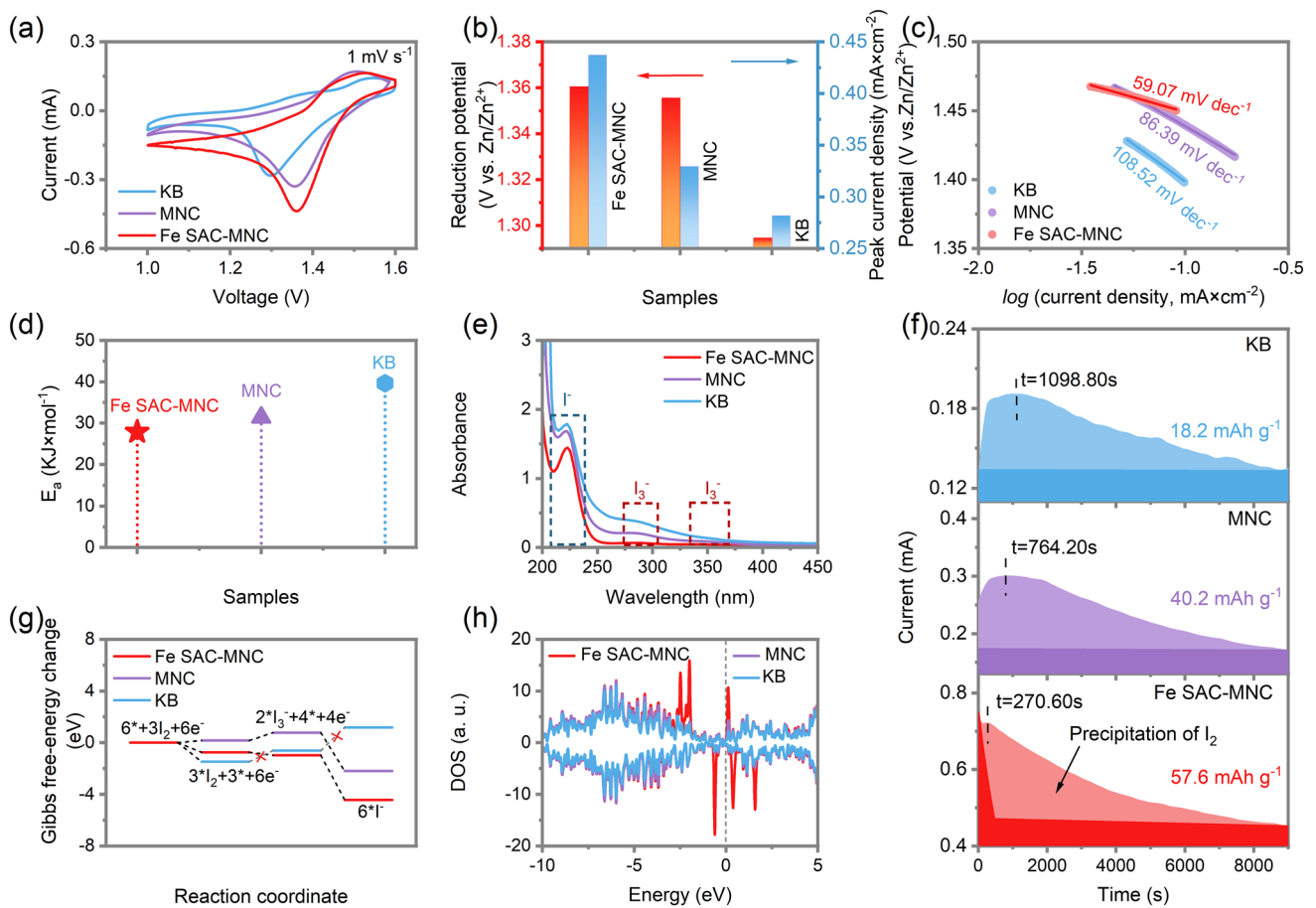


Fig. 2 **a** CV curves of the Fe SAC-MNC, MNC and KB electrocatalysts in 2 M ZnSO₄+0.02 M I₂ solution in two-electrode configuration at 1 mV s⁻¹. **b** The I₂ reduction potential and peak current density determined from CV curves. **c** Corresponding Tafel plots from CV curves. **d** Comparison of activation energies of Fe SAC-MNC, MNC and KB for IRR. **e** UV-vis absorption spectra of electrolytes for Fe SAC-MNC, MNC and KB after sufficient IRR. **f** Potentiostatic discharge curves of I₂ solution at 1.34 V on the surfaces of Fe SAC-MNC, MNC and KB cathodes. **g** Gibbs free-energy graphs of I₂ reduction reaction of Fe SAC-MNC, MNC and KB. **h** Density of states (DOS) for Fe SAC-MNC, MNC and KB hosts

predicates the smaller activation energy (E_a). The specific E_a is calculated using the following Arrhenius equation:

$$\frac{1}{R_{ct}} = A \exp\left(\frac{-E_a}{RT}\right) \quad (1)$$

where R_{ct} is the charge transfer resistance, E_a is the activation energy, T is the temperature and R is the gas constant. The E_a of IRR by Fe SAC-MNC is calculated to be 27.878 kJ mol⁻¹, smaller than that of MNC (31.386 kJ mol⁻¹) and (39.654 kJ mol⁻¹), representing the super-fast kinetic of electrocatalytic IRR under existing of Fe SAC (Fig. 2d). In addition, the UV-vis spectroscopy is utilized to detect the formation of I^- and I_3^- in the electrolyte (2 M ZnSO₄) during I^-/I_2 reaction with Fe SAC-MNC, MNC and KB electrocatalysts employed, respectively. As

shown in Fig. 2e, after sufficient IRR, the apparent peak at 226 nm is indexed to form I^- , while the two peaks at 288 and 355 nm are ascribed to the formation of I_3^- in MNC and KB. In comparison, no I_3^- formed in Fe SAC-MNC catalyzed IRR, further certifying the forceful physio/chemical affinity of Fe SAC-MNC with iodine species and totality of reaction from I_2 to I^- . The rate of I_2 precipitation on the electrode matrix is another key indicator for Zn-I₂ batteries to evaluate the conversion kinetic of I_3^-/I_2 [35, 44]. The potentiostatic discharge measurement is performed to probe the electrochemical deposition from solution I_3^- to solid I_2 at 1.34 V (Fig. 2f). The dark and light color depict the reduction and precipitation of I_2 , respectively. The Fe SAC-MNC electrode achieves the highest current peak at the shortest time (0.72 mA after 270.60 s), in comparison to the MNC (0.29 mA after 764.20 s) and KB (0.19 mA after 1,098.80 s)

electrode. The capacities of the I_2 precipitation on Fe SAC-MNC, MNC and KB are determined to be 57.6, 40.2 and 18.2 mAh g^{-1} , affirming the remarkable nucleation of I_2 at Fe SAC-MNC electrode during same period (9000 s).

The DFT calculation is further performed to evaluate the spontaneity of I_2 species conversion on the active centers of Fe SAC-MNC. The lower the Gibbs free energy (ΔG) represents the deeper spontaneity trends and the faster reaction kinetics [34]. The I_2/I^- redox reactions often proceed in two steps of $I_2 + 2/3 e^- \leftrightarrow 2/3 I_3^-$ and $I_3^- + 2e^- \leftrightarrow 3I^-$, where the latter one is the rate-determining step for whole IRR. The ΔG value for I_3^-/I^- is -3.4658 eV for Fe SAC-MNC electrocatalyst, which is lower than -2.973 eV for MNC and 1.7816 eV for KB electrocatalysts (Fig. 2h, Table S2). The results manifest the fastest kinetic conversion of I_2 on the Fe SAC-MNC host in electrochemical process, consistent with above experimental outcome. The I^- oxidation to I_2 is evaluated by the Zn-I decomposition process visualizing by the ab initio molecular dynamics simulation. In comparison to the chemical inertia hosts of MNC and KB, the radial distribution function curves of Zn-I on Fe SAC-MNC show larger Zn-I bond length (Fig. S9), indicating the easy break of Zn-I bond on Fe SAC-MNC. In contrast to MNC and KB, the Fe SAC-MNC is quite more metallic for a higher DOS at the Fermi level, giving evidence of satisfactory electrical conductivity of Fe SAC-MNC to markedly enhance the fast electrochemical reaction between I^- and I_2 (Fig. 2h). As a result, abundant order mesoporous MNC improve the physical confinement for $I_2/I^-/I_3^-$ species and the Fe SAC boost the super-fast kinetic for I_2/I^- redox reactions.

2.3 Zn// I_2 Batteries with Fast Redox Kinetics and High Capacity

The current density (i) of cathodic and anodic reaction against the square roots of scan rates ($v^{1/2}$) are derived from the CV curves at different scan rate (Fig. S10). The linear relationship declares that the redox reactions are controlled by mass diffusion transport. The resulting proton diffusivity (D_H) values are calculated by the Randle-Sevcik equation for Fe SAC-MNC/ I_2 , MNC/ I_2 and KB/ I_2 . The D_H values of Fe SAC-MNC/ I_2 is $1.83 \times 10^{-10} \text{ cm}^2 \text{ s}^{-1}$, larger than $9.05 \times 10^{-11} \text{ cm}^2 \text{ s}^{-1}$ for MNC/ I_2 and $8.36 \times 10^{-11} \text{ cm}^2 \text{ s}^{-1}$ for KB/ I_2 which declares that Fe SAC is a key point for I^-/I_2 redox reaction to boost iodine utilization and reaction

kinetics (Fig. 3a). The galvanostatic intermittent titration technique (GITT) are further performed to confirmed diffusion coefficient of different cathodes (Fig. 3b). A relatively higher Zn^{2+} diffusion coefficient is received for Fe SAC-MNC/ I_2 in almost all the discharge/charge states (Regions 1–3). The Fe SAC-MNC/ I_2 cathode exhibits persistent high proton D_H , even if at 75% depth of discharge (DOD) [45]. The charge transfer resistance is another important criterion for judging redox reaction kinetic. The Nyquist plot diagram exhibits a smallest charge transfer resistance (R_{ct} , 48.12 Ω) of Fe SAC-MNC/ I_2 , compared with that of the MNC/ I_2 (68.65 Ω) and KB/ I_2 (77.06 Ω), which can be attributed to the introduction of Fe SAC (Fig. 3c). The characteristic frequency (f_{max}) of Fe SAC-MNC/ I_2 cathode is 1,181.6 Hz (0.8467 ms) suggesting a faster charge response than that of MNC/ I_2 cathode (740.5 Hz, 1.35 ms) and KB/ I_2 cathode (586.3 Hz, 1.71 ms). Both enhanced proton diffusivity and boosted charge response accounts for the role of Fe SAC for I_2/I^- redox conversion.

The cyclic voltammetry (CV) curves of Fe SAC-MNC/ I_2 , MNC/ I_2 and KB/ I_2 electrode are used to evaluate the electrocatalytic effects at 5 mV s^{-1} from 0.45–1.65 V. In comparison of the cathodic and anodic peak for MNC/ I_2 (1.291 and 1.148 V) and KB/ I_2 (1.513 and 1.179 V), the Fe SAC-MNC/ I_2 displayed a pair of strongest current peaks for I_2/I^- redox reaction at 1.414 and 1.191 V, respectively (Fig. 3d). The higher intensity of current peaks and larger enclosed area indicate the faster redox reaction kinetic and higher capacity of Fe SAC-MNC/ I_2 , which is attributed to fast I_2/I^- redox reactions and high active I_2 loading. The CV curves at different scan rate indicates the distinguished electrochemical reversibility (Fig. S10). As shown in Fig. 3e, the Fe SAC-MNC/ I_2 cathode exhibits a smallest Tafel slope of 75.25 mV dec^{-1} , compared with MNC/ I_2 (82.28 mV dec^{-1}) and KB/ I_2 (89.72 mV dec^{-1}) cathodes, which reveals the prominent improvement of I_2/I^- redox reaction kinetic by Fe SAC active sites.

Inspired by the physical confinement structure of MNC and chemical adsorption/catalytic of Fe SAC, the Zn//Fe SAC-MNC/ I_2 battery shows preponderant capacity of 188.21, 180.92, 175.96, 168.53, 163.32, 151.33 and 139.60 mAh g^{-1} at 0.3, 0.5, 1, 3, 5, 10, and 15 A g^{-1} , which are almost twice and three times as much as Zn//MNC/ I_2 and Zn//KB/ I_2 battery (Fig. 3f), respectively. At the higher current density, the importance of electrocatalyst can be highlighted. Encouragingly, the Fe SAC-MNC/ I_2 cathode achieves high

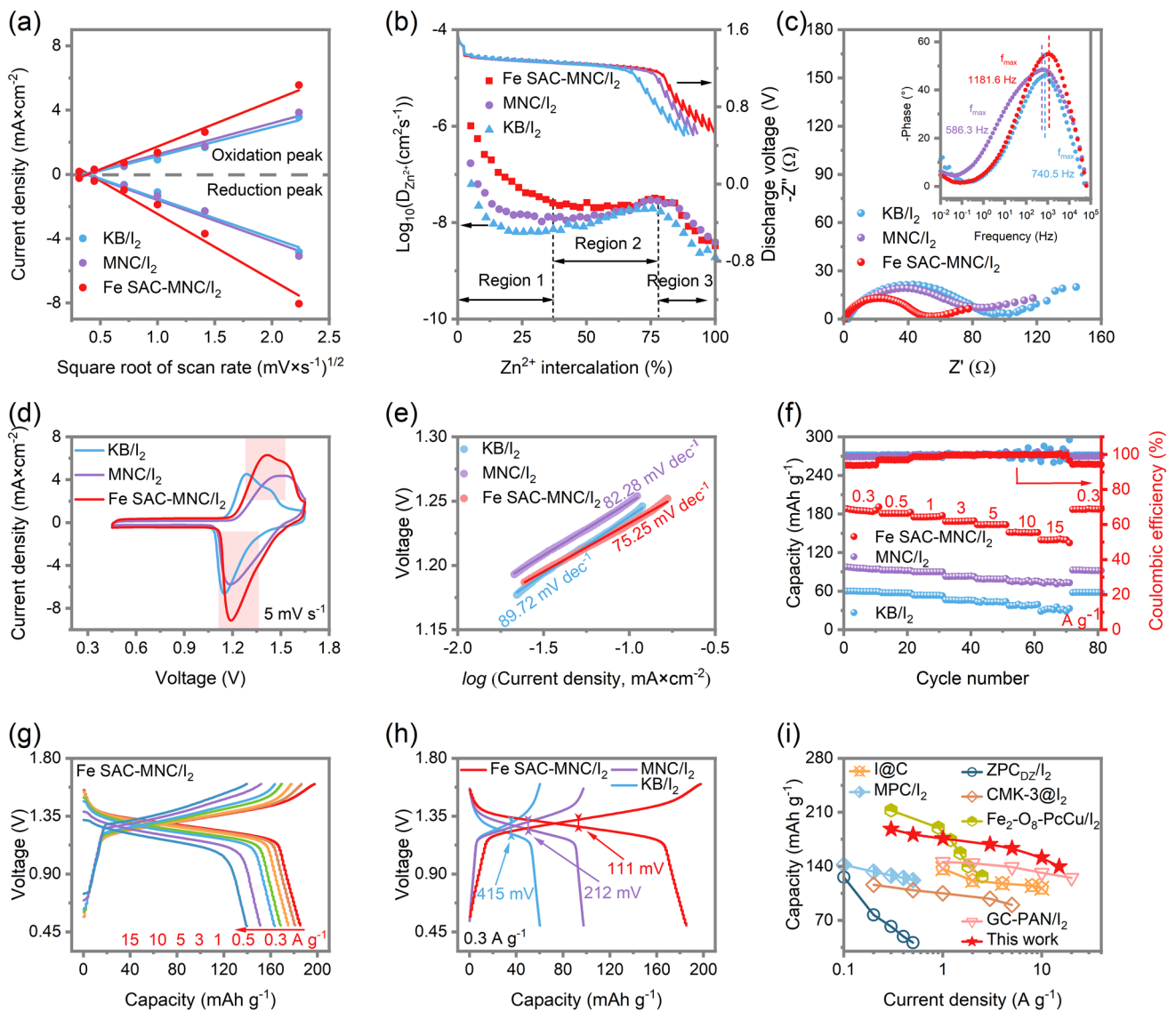


Fig. 3 **a** Linear correlation between the peak current and the square root of the scan rate for Fe SAC-MNC/I₂, MNC/I₂ and KB/I₂. **b** GITT curves and diffusivity versus DOD. **c** Nyquist plots. Inset: Bode plots of the (R_{ct}Q_{dl}) parallel components. **d** CV curves comparison among Fe SAC-MNC/I₂, MNC/I₂ and KB/I₂. **e** Corresponding Tafel plots. **f** Rate capability of Fe SAC-MNC/I₂, MNC/I₂ and KB/I₂ at various rate of 0.3–15 A g⁻¹. **g** GCD curves of Fe SAC-MNC/I₂ at different rates. **h** GCD curves comparison between Fe SAC-MNC/I₂, MNC/I₂ and KB/I₂. **i** Ragone plot of this work compared to the previously reported metal-I₂ batteries for capacity and current density [29, 30, 32, 34, 41, 53]

capacity of 139.60 mAh g⁻¹ and stable coulomb efficiency of 99.88% at 15 A g⁻¹, much higher than that of (73.89 mAh g⁻¹) and KB/I₂ (35.52 mAh g⁻¹) cathodes. It's worth noting that the capacity of Zn||Fe SAC-MNC/I₂ battery at such high rate (15 A g⁻¹) outperforms most previous works [46–49]. In contrast, with current density increased from 0.3 to 15 A g⁻¹, the CE curves of Zn||KB/I₂ battery become greatly unstable, suggesting deficient I₂/I⁻ conversion reactions. The galvanostatic charge/discharge (GCD) curves of

Zn||Fe SAC-MNC/I₂ battery are displayed in Fig. 3g at different rate (0.3–15 A g⁻¹), being company with Zn||MNC/I₂ and Zn||KB/I₂ battery (Fig. S11). Along with the increasing of rate, the capacities of Fe SAC-MNC/I₂ cathode show a small decay with uniformly clear charge/discharge plateaus, which is consistent with the CV curves (Fig. S4). Meanwhile, the Zn||Fe SAC-MNC/I₂ battery displays the smallest electrochemical polarization (111 vs. 212 mV for MNC/I₂ and 415 mV for KB/I₂), suggesting the extinguished active

I_2 utilization and outstanding redox reaction kinetic (Fig. 3h) [50]. That illustrates the Fe SAC active sites have prominent effect for the decrease of activation energy and the acceleration of charge transport in I^-/I_2 redox reaction. The Zn- I_2 battery using Fe SAC-MNC host achieves a high energy density of $190.47 \text{ Wh kg}^{-1}$ at 650.09 W kg^{-1} , overmatching recently reported Zn- I_2 , Fe- I_2 , K- I_2 and Cu- I_2 batteries (Fig. S12) [29, 37, 51, 52]. Notably, as shown in Fig. 3i, the aqueous Zn batteries using the Fe SAC-MNC/ I_2 cathode achieve higher capacity at different current density ($0.3\text{--}15 \text{ A g}^{-1}$) than mostly reported metal-iodine batteries, demonstrating its fast reaction kinetics and high active I_2 utilization [29, 30, 32, 34, 41, 53].

Using the host of Fe SAC-MNC, the Zn// I_2 battery displayed super-stable cycle performance and super-long lifespan at a high current density of 5 A g^{-1} with initial capacity retention of 80.5% (from 198.5 to 159.7 mAh g^{-1}) even over 50,000 cycles (Fig. 4a). Although the Zn//MNC/ I_2 battery showed more stable cycle performance than KB/ I_2 //Zn battery, it is still dissatisfied for limited capacity (68.49 to 46.26 mAh g^{-1}) and lifespan (only 7,000 cycles). The above results confirm the excellent electrocatalyst ability of Fe SAC and strong iodine species adsorption of MNC as I_2 host. In I_2 XPS high resolution spectra, two peaks clearly located at 619.2 and 630.7 eV are ascribed to I-C and I-O bond, respectively (Fig. 4b). After fully discharge to 0.5 V, the position of two peaks slightly shift to 619.1 and 630.6 eV, respectively. Then two peaks shift to initial position at fully charge to 1.6 V, revealing highly reversible conversion reaction of I_2/I^- . In the metal// I_2 battery, the shuttles of I_2 and its reaction production (I^- and I_3^-) to metal anode not only intensify capacity decay, but also generate the oxygen evolution reaction (OER) and metal anode corrosion [10, 54, 55]. The surface of the Zn anode after cycling tests in Zn//Fe SAC-MNC/ I_2 , Zn//MNC/ I_2 and Zn//KB/ I_2 cells are visualized by SEM images. As illustrated in Fig. 4c, the surface of Zn anode with KB/ I_2 cathode is seriously attacked by the iodine species to engender many huge holes. Utilizing MNC/ I_2 cathode, although the surface of Zn anode appears less holes, we still clearly observe some Zn corrosion. The loose Zn anode with disorganized holes prejudices the transportation of electron and ions [56–58]. In comparison, benefitting from the physio/chemical adsorption of Fe SAC-MNC for iodine species and thorough-paced I_2/I^- conversion, the Zn anode in Zn//Fe SAC-MNC/ I_2 cell maintains smooth surface and dense Zn deposits. The comparisons in aspect of I_2

weight content, capacity, cycle number, capacity retention and energy density are conducted to elaborate the superiority of Fe SAC-MNC host for Zn// I_2 batteries (Fig. 4d) [29, 30, 33]. It is observed that the Zn//Fe SAC-MNC/ I_2 batteries present distinguished superiority in all respects.

In light of high-performance coin-cell Zn//Fe SAC-MNC/ I_2 batteries, a pouch cell with a high areal Fe SAC-MNC/ I_2 loading to 3.0 mg cm^{-2} is assembled in a single-piece cathode. The battery achieves a high capacity of 36.88 mAh and maintains 30.37 mAh after 200 cycles (Fig. 4e). Meanwhile, the pouch-type cell advocates stable voltage profile and maintain minimal voltage polarization after 200 charge/discharge cycles (Fig. 4f). The results suggest a high iodine utilization and stable cycling performance even under high iodine weight content and mass loading, which supporting the effectiveness of our “confinement-catalysis” strategy in immobilizing $I_2/I_3^-/I^-$ species, converting I_2/I^- and eliminating Zn metal corrosion.

2.4 Fast Kinetics of $I^-/I^0/I^+$ Four Electron Redox Reaction

To further examine the functions of Fe SAC-MNC host in catalyzing the I^0/I^+ redox reaction and stabling the confinement of I^0/I^+ species, according to previous works, the double salt electrolyte (19 M $ZnCl_2$ and 19 M $LiCl$) adding with 8 M Acetonitrile (ACN) is selected to activate I^0/I^+ redox [1, 59]. Two pairs of redox peaks are clearly observed in CV curves of Zn//Fe SAC-MNC/ I_2 , Zn//MNC/ I_2 and Zn//KB/ I_2 batteries, representing the I^0/I^+ and I^0/I^- redox reactions (Fig. 5a). The Zn//Fe SAC-MNC/ I_2 shows two redox more obvious peaks at 1.30/1.18 V and 1.87/1.65 V and largest closed area. Meanwhile, it shows smallest the Tafel slope of $94.18 \text{ mV dec}^{-1}$, in comparison to Zn//MNC/ I_2 ($115.24 \text{ mV dec}^{-1}$) and Zn//KB/ I_2 ($136.06 \text{ mV dec}^{-1}$) (Fig. 5b). The results illustrate the fast $I^-/I^0/I^+$ redox kinetics and sufficient iodine utilization of using Fe SAC-MNC host for four-electron transfer Zn// I_2 batteries. The CV curves of Fe SAC-MNC/ I_2 cathode at different scan rates of $0.1\text{--}3 \text{ mV s}^{-1}$ revealed the stable and reversible conversion reaction, compared MNC/ I_2 and KB/ I_2 cathode (Fig. S13). For a more direct observation, the Charge/discharge voltage profiles of three cathodes at 0.5 A g^{-1} are distinguished in Fig. 5c, in which the two discharge platforms of Zn//Fe SAC-MNC/ I_2 battery located at 1.28 and 1.71 V correspond to the I^-/I^0 and I^0/I^+ redox reactions, respectively. The Zn//Fe SAC-MNC/ I_2

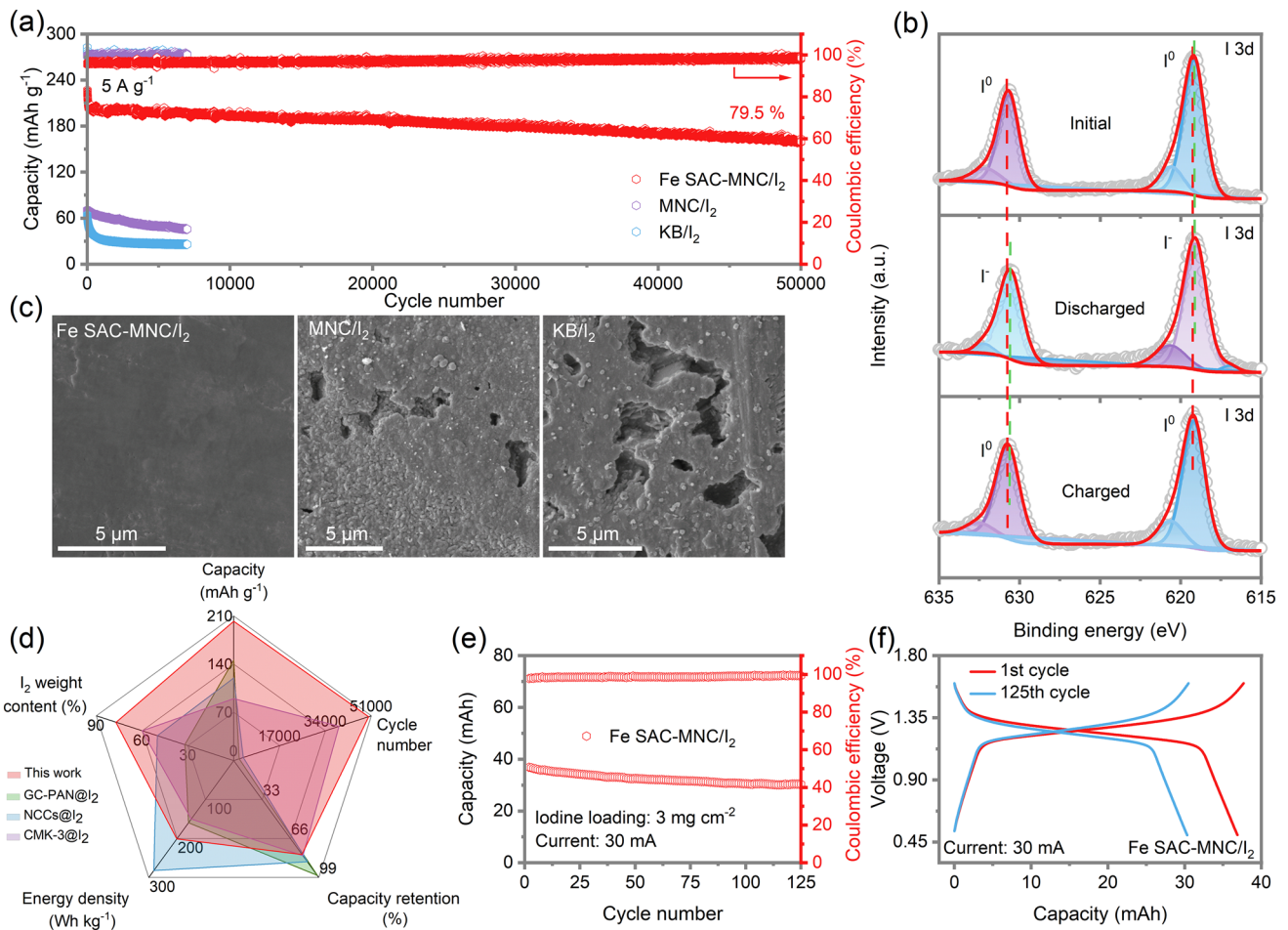


Fig. 4 **a** Long-term cycling performance the Zn||Fe SAC-MNC/I₂, Zn||MNC/I₂ and Zn||KB/I₂ batteries at 5 A g⁻¹. **b** High resolution XPS spectra of I 3d at initial, discharged and charged states. **c** SEM images of Zn anode after cycling in the Zn||Fe SAC-MNC/I₂, Zn||MNC/I₂ and Zn||KB/I₂ batteries. **d** Comparison of Zn||Fe SAC-MNC/I₂ batteries with other Zn||I₂ batteries in aspect of I₂ weight content, capacity, cycle number, capacity retention and energy density [29, 30, 33]. **e** Cycle performance of 300-mg-iodine pouch cell using Fe SAC-MNC/I₂ cathode and **f** the charge/discharge curves of the 1st cycle and the 200th cycle

battery delivers highest discharge capacity of 230 mAh g⁻¹ at 0.5 A g⁻¹ and 109.49 mAh g⁻¹ at high current density of 10 A g⁻¹, much higher than that of Zn||MNC/I₂ battery (48.18 mAh g⁻¹ at 10 A g⁻¹), demonstrating the distinguish electrocatalytic capability of Fe SAC-MNC/I₂ cathode to realize fast four electrons redox reactions (Figs. 5d and S14). In contrast, with the current density increased to 5 A g⁻¹, the Zn||KB/I₂ battery fails, due to inactive single-ingredient and disordered pore structure of KB host. The KB hosts cannot support four electrons transfer redox under high current density, giving rise to “necrosis”. As the current

density increasing, the interface of electrode–electrolyte will absorb most electrolyte ions. Hence, the capacity may decay if the number of interfacial charges is not enough, proving the excellent catalysis of Fe SAC for I⁻/I₀/I⁺ redox reaction again. Meanwhile, the Zn||Fe SAC-MNC/I₂ battery achieves the long lifespan of 500 cycles with the capacity of 237.35 mAh g⁻¹ delivered at 1 A g⁻¹, which is twice as much as Zn||MNC/I₂ and Zn||KB/I₂ batteries, at actualizing the CE of ~ 100% (Fig. 5e), revealing Fe SAC effectively accelerates the charge transfer in four-electron redox reaction for the improvement of iodine utilization, specific capacity and capacity retention.

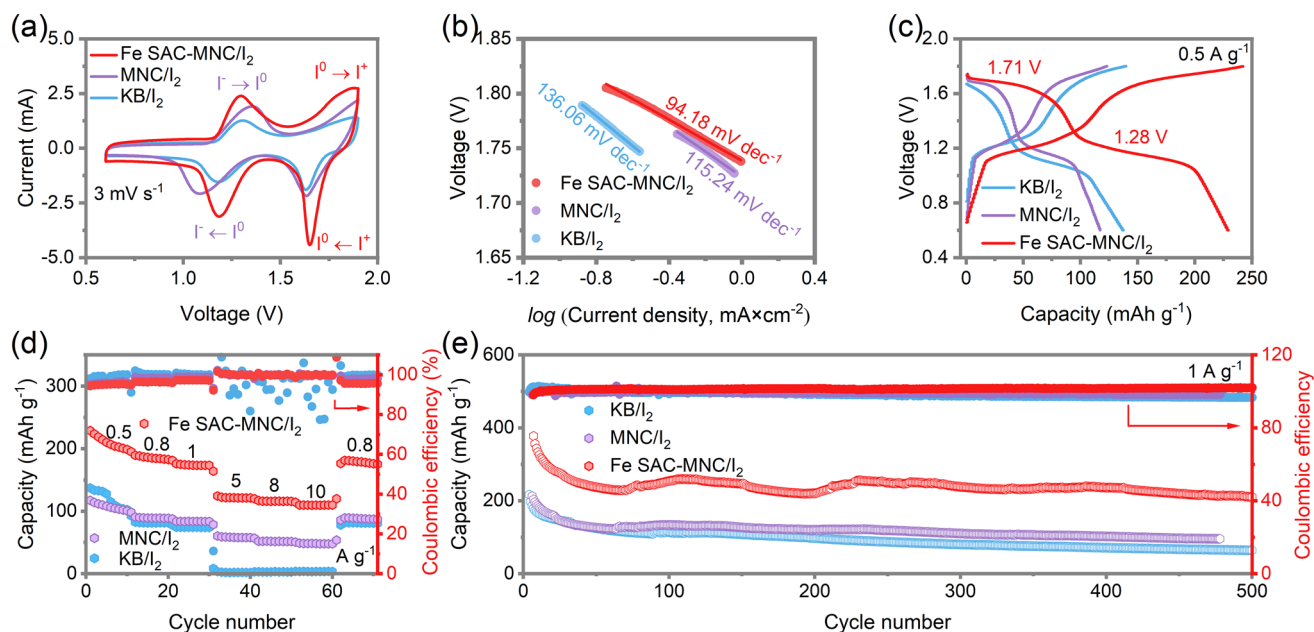


Fig. 5 **a** Cyclic voltammetry (CV) profiles of Zn||Fe SAC-MNC/I₂, Zn||MNC/I₂ and Zn||KB/I₂ batteries with selected electrolyte at 3 mV s⁻¹ and **b** Corresponding Tafel plots from CV curves. **c** Charge and discharge voltage profiles of various cathodes at 0.5 A g⁻¹. **d** Rate capability of Zn||Fe SAC-MNC/I₂, Zn||MNC/I₂ and Zn||KB/I₂ batteries at various current density of 0.5–10 A g⁻¹. **e** Long-term cycling performance of the Zn||Fe SAC-MNC/I₂, Zn||MNC/I₂ and Zn||KB/I₂ batteries at 1 A g⁻¹

3 Conclusion

In summary, we have exhibited that a catalytic iodine host with Fe–N–C SAC implanted into ordered mesoporous matrix implement high iodine utilization, fast redox reaction kinetics, long-term cyclic lifespan, no shuttle effects in Zn||I₂ batteries. The interconnected microporous carbon framework promotes electron/ion transportation. While the Fe–N–C SAC catalytic sites boost the iodine utilization and I⁻/I₂/I⁺ redox reaction kinetics under high iodine loading. Meanwhile, the catalytic host can effectively confine and convert iodine/polyiodide intermediators to suppress Zn anode corrosion. As a result, the aqueous Zn||I₂ batteries based I₂/I⁻ delivers high capacity of 188.2 mAh g⁻¹ at current density of 0.3 A g⁻¹, high-rate capability with a capacity of 139.6 mAh g⁻¹ delivered at high current density of 15 A g⁻¹ and ultra-long lifespan over 50,000 cycles with 80.5% initial capacity retained at 5 A g⁻¹ under high iodine loading of 76.72 wt%. Meanwhile, the four-electron-transfer Zn||I₂ batteries achieve 230 mAh g⁻¹ at 0.5 A g⁻¹ and 109.49 mAh g⁻¹ at high current density of 10 A g⁻¹. Our strategy bridges the gap between the high specific energy of Zn||I₂ batteries

in coin-cell configuration and their realization in practical device-level systems.

Acknowledgements This work was supported by the National Key Research and Development Project (2020YFC1521900 and 2020YFC1521904) and the Shaanxi Provincial Science Foundation (2021GXLH-01-11). We would also like to thank National Natural Science Foundation of China (52202299) and Analytical & Testing Center of Northwestern Polytechnical University (2022T006).

Funding Open access funding provided by Shanghai Jiao Tong University.

Conflict of Interest The authors declare no interest conflict. They have no known competing financial interests or personal relationships that could have appeared to influence the work reported in this paper.

Open Access This article is licensed under a Creative Commons Attribution 4.0 International License, which permits use, sharing, adaptation, distribution and reproduction in any medium or format, as long as you give appropriate credit to the original author(s) and the source, provide a link to the Creative Commons licence, and indicate if changes were made. The images or other third party material in this article are included in the article's Creative Commons licence, unless indicated otherwise in a credit line to the material. If material is not included in the article's Creative Commons licence and your intended use is not permitted by statutory regulation or exceeds the permitted use, you will need to obtain

permission directly from the copyright holder. To view a copy of this licence, visit <http://creativecommons.org/licenses/by/4.0/>.

Supplementary Information The online version contains supplementary material available at <https://doi.org/10.1007/s40820-023-01093-7>.

References

1. Y. Zou, T. Liu, Q. Du, Y. Li, H. Yi et al., A four-electron Zn-I₂ aqueous battery enabled by reversible I⁻/I₂/I⁺ conversion. *Nat. Commun.* **12**(1), 170 (2021). <https://doi.org/10.1038/s41467-020-20331-9>
2. B. Li, Z. Nie, M. Vijayakumar, G. Li, J. Liu et al., Ambipolar zinc-polyiodide electrolyte for a high-energy density aqueous redox flow battery. *Nat. Commun.* **6**(1), 6303 (2015). <https://doi.org/10.1038/ncomms7303>
3. D. Lin, Y. Li, Recent advances of aqueous rechargeable zinc-iodine batteries: challenges, solutions, and prospects. *Adv. Mater.* **34**(23), 2108856 (2022). <https://doi.org/10.1002/adma.202108856>
4. C. Bai, F. Cai, L. Wang, S. Guo, X. Liu et al., A sustainable aqueous Zn-I₂ battery. *Nano Res.* **11**(7), 3548–3554 (2018). <https://doi.org/10.1007/s12274-017-1920-9>
5. H. Pan, B. Li, D. Mei, Z. Nie, Y. Shao et al., Controlling solid–liquid conversion reactions for a highly reversible aqueous zinc–iodine battery. *ACS Energy Lett.* **2**(12), 2674–2680 (2017). <https://doi.org/10.1021/acseenergylett.7b00851>
6. C. Prehal, H. Fitzek, G. Kothleitner, V. Presser, B. Gollas et al., Persistent and reversible solid iodine electrodeposition in nanoporous carbons. *Nat. Commun.* **11**(1), 4838 (2020). <https://doi.org/10.1038/s41467-020-18610-6>
7. X. Li, X. Wang, L. Ma, W. Huang, Solvation structures in aqueous metal-ion batteries. *Adv. Energy Mater.* **12**(37), 2202068 (2022). <https://doi.org/10.1002/aenm.202202068>
8. W. Shang, Q. Li, F. Jiang, B. Huang, J. Song, B. Zn et al., I₂ battery's performance by coating a zeolite-based cation-exchange protecting layer. *Nano-Micro Lett.* **14**(1), 82 (2022). <https://doi.org/10.1007/s40820-022-00825-5>
9. Z. Wang, J. Huang, Z. Guo, X. Dong, Y. Liu et al., A metal-organic framework host for highly reversible dendrite-free zinc metal anodes. *Joule* **3**(5), 1289–1300 (2019). <https://doi.org/10.1016/j.joule.2019.02.012>
10. H. Yang, Y. Qiao, Z. Chang, H. Deng, P. He et al., A metal-organic framework as a multifunctional ionic sieve membrane for long-life aqueous zinc–iodide batteries. *Adv. Mater.* **32**(38), 2004240 (2020). <https://doi.org/10.1002/adma.202004240>
11. Y. Yang, S. Liang, B. Lu, J. Zhou, Eutectic electrolyte based on n-methylacetamide for highly reversible zinc–iodine battery. *Energy Environ. Sci.* **15**(3), 1192–1200 (2022). <https://doi.org/10.1039/D1EE03268B>
12. X. Wang, X. Li, H. Fan, L. Ma, Solid electrolyte interface in Zn-based battery systems. *Nano-Micro Lett.* **14**(1), 205 (2022). <https://doi.org/10.1007/s40820-022-00939-w>
13. F. Hu, M. Li, G. Gao, H. Fan, L. Ma, The gel-state electrolytes in zinc-ion batteries. *Batteries* **8**(11), 214 (2022). <https://doi.org/10.3390/batteries8110214>
14. R. Zhao, X. Dong, P. Liang, H. Li, T. Zhang et al., Prioritizing hetero-metallic interfaces *via* thermodynamics inertia and kinetics zincophilia metrics for tough Zn-based aqueous batteries. *Adv. Mater.* (2023). <https://doi.org/10.1002/adma.202209288>
15. Z. Wang, L. Dong, W. Huang, H. Jia, Q. Zhao et al., Simultaneously regulating uniform Zn²⁺ flux and electron conduction by MOF/rGo interlayers for high-performance Zn anodes. *Nano-Micro Lett.* **13**(1), 73 (2021). <https://doi.org/10.1007/s40820-021-00594-7>
16. Y. Yang, S. Liang, J. Zhou, Progress and prospect of the zinc–iodine battery. *Curr. Opin. Electrochem.* **30**, 100761 (2021). <https://doi.org/10.1016/j.coelec.2021.100761>
17. J. Liu, W. Zhou, R. Zhao, Z. Yang, W. Li et al., Sulfur-based aqueous batteries: electrochemistry and strategies. *J. Am. Chem. Soc.* **143**(38), 15475–15489 (2021). <https://doi.org/10.1021/jacs.1c06923>
18. T. Liu, H. Wang, C. Lei, Y. Mao, H. Wang et al., Recognition of the catalytic activities of graphitic n for zinc-iodine batteries. *Energy Stor. Mater.* **53**, 544–551 (2022). <https://doi.org/10.1016/j.ensm.2022.09.028>
19. H. Ge, X. Feng, D. Liu, Y. Zhang, Recent advances and perspectives for Zn-based batteries: Zn anode and electrolyte. *Nano Res. Energy* **2**, e9120039 (2023). <https://doi.org/10.26599/NRE.2023.9120039>
20. W. Wu, C. Li, Z. Wang, H.-Y. Shi, Y. Song et al., Electrode and electrolyte regulation to promote coulombic efficiency and cycling stability of aqueous zinc-iodine batteries. *Chem. Eng. J.* **428**, 131283 (2022). <https://doi.org/10.1016/j.cej.2021.131283>
21. Y. Tian, S. Chen, S. Ding, Q. Chen, J. Zhang, A highly conductive gel electrolyte with favorable ion transfer channels for long-lived zinc–iodine batteries. *Chem. Sci.* **14**(2), 331–337 (2023). <https://doi.org/10.1039/D2SC06035C>
22. S. Huang, S. He, H. Qin, X. Hou, Oxygen defect hydrated vanadium dioxide/graphene as a superior cathode for aqueous Zn batteries. *ACS Appl. Mater. Interfaces* **13**(37), 44379–44388 (2021). <https://doi.org/10.1021/acsmi.1c12653>
23. Y. Li, M. Zhu, D.D. Karnaushenko, F. Li, J. Qu et al., Micro-batteries with twin-swiss-rolls redefine performance limits in the sub-square millimeter range. *Nanoscale Horiz.* **8**(1), 127–132 (2022). <https://doi.org/10.1039/d2nh00472k>
24. Y. Li, M. Zhu, V.K. Bandari, D.D. Karnaushenko, D. Karnaushenko et al., On-chip batteries for dust-sized computers. *Adv. Energy Mater.* **12**(13), 2103641 (2022). <https://doi.org/10.1002/aenm.202103641>
25. X.Y. Xie, L.S. Peng, H.Z. Yang, G.I.N. Waterhouse, L. Shang et al., Mil-101-derived mesoporous carbon supporting highly exposed Fe single-atom sites as efficient oxygen reduction



- reaction catalysts. *Adv. Mater.* **33**(23), 2101038 (2021). <https://doi.org/10.1002/adma.202101038>
26. S. Chen, X. Liang, S. Hu, X. Li, G. Zhang et al., Inducing Fe 3d electron delocalization and spin-state transition of FeN₄ species boosts oxygen reduction reaction for wearable zinc–air battery. *Nano-Micro Lett.* **15**(1), 47 (2023). <https://doi.org/10.1007/s40820-023-01014-8>
27. X. Zheng, Y. Zhou, X. Yan, K.-H. Lam, X. Hou, Vanadium oxide with elevated interlayers for durable aqueous hybrid Li⁺/Zn²⁺ batteries. *ACS Appl. Energy Mater.* **5**(7), 9070–9078 (2022). <https://doi.org/10.1021/acsaem.2c01512>
28. D.L. Yu, A. Kumar, T.A. Nguyen, M.T. Nazir, G. Yasin, High-voltage and ultrastable aqueous zinc-iodine battery enabled by N-doped carbon materials: revealing the contributions of nitrogen configurations. *ACS Sustain. Chem. Eng.* **8**(36), 13769–13776 (2020). <https://doi.org/10.1021/acssuschemeng.0c04571>
29. Q. Guo, H. Wang, X. Sun, Y.N. Yang, N. Chen et al., In situ synthesis of cathode materials for aqueous high-rate and durable Zn–I₂ batteries. *ACS Mater. Lett.* **4**(10), 1872–1881 (2022). <https://doi.org/10.1021/acsmaterialslett.2c00608>
30. L.Q. Zhang, M.J. Zhang, H.L. Guo, Z.H. Tian, L.F. Ge et al., A universal polyiodide regulation using quaternization engineering toward high value-added and ultra-stable zinc-iodine batteries. *Adv. Sci.* **9**(13), 2105598 (2022). <https://doi.org/10.1002/advs.202105598>
31. H.K. Machhi, K.K. Sonigara, S.N. Bariya, H.P. Soni, S.S. Soni, Hierarchically porous metal-organic gel hosting catholyte for limiting iodine diffusion and self-discharge control in sustainable aqueous zinc-I₂ batteries. *ACS Appl. Mater. Interfaces* **13**(18), 21426–21435 (2021). <https://doi.org/10.1021/acsaami.1c03812>
32. J. Xu, J. Wang, L. Ge, J. Sun, W. Ma et al., ZIF-8 derived porous carbon to mitigate shuttle effect for high performance aqueous zinc-iodine batteries. *J. Colloid Interface Sci.* **610**, 98–105 (2022). <https://doi.org/10.1016/j.jcis.2021.12.043>
33. W.F. Liu, P.G. Liu, Y.H. Lyu, J. Wen, R. Hao et al., Advanced Zn-I₂ battery with excellent cycling stability and good rate performance by a multifunctional iodine host. *ACS Appl. Mater. Interfaces* **14**(7), 8955–8962 (2022). <https://doi.org/10.1021/acsaami.1c21026>
34. F. Wang, Z. Liu, C. Yang, H. Zhong, G. Nam et al., Fully conjugated phthalocyanine copper metal-organic frameworks for sodium-iodine batteries with long-time-cycling durability. *Adv. Mater.* **32**(4), 1905361 (2020). <https://doi.org/10.1002/adma.201905361>
35. K. Wang, J.-B. Le, S.-J. Zhang, W.-F. Ren, J.-M. Yuan et al., A renewable biomass-based lignin film as an effective protective layer to stabilize zinc metal anodes for high-performance zinc-iodine batteries. *J. Mater. Chem. A* **10**(9), 4845–4857 (2022). <https://doi.org/10.1039/d1ta10170f>
36. L. Ma, Y. Ying, S. Chen, Z. Huang, X. Li et al., Electrocatalytic iodine reduction reaction enabled by aqueous zinc-iodine battery with improved power and energy densities. *Angew. Chem. Int. Ed.* **60**(7), 3791–3798 (2021). <https://doi.org/10.1002/anie.202014447>
37. C. Bai, H. Jin, Z. Gong, X. Liu, Z. Yuan, A high-power aqueous rechargeable Fe-I₂ battery. *Energy Stor. Mater.* **28**, 247–254 (2020). <https://doi.org/10.1016/j.enstm.2020.03.010>
38. H. Park, R.K. Bera, R. Ryoo, Microporous 3d graphene-like carbon as iodine host for zinc-based battery-supercapacitor hybrid energy storage with ultrahigh energy and power densities. *Adv. Energy Sustain. Res.* **2**(10), 2100076 (2021). <https://doi.org/10.1002/aesr.202100076>
39. L. Xiang, S. Yuan, F. Wang, Z. Xu, X. Li et al., Porous polymer cubosomes with ordered single primitive bicontinuous architecture and their sodium–iodine batteries. *J. Am. Chem. Soc.* **144**(34), 15497–15508 (2022). <https://doi.org/10.1021/jacs.2c02881>
40. X. Zeng, X. Meng, W. Jiang, J. Liu, M. Ling et al., Anchoring polyiodide to conductive polymers as cathode for high-performance aqueous zinc–iodine batteries. *ACS Sustain. Chem. Eng.* **8**(38), 14280–14285 (2020). <https://doi.org/10.1021/acssuschemeng.0c05283>
41. Y. Hou, F. Kong, Z. Wang, M. Ren, C. Qiao et al., High performance rechargeable aqueous zinc-iodine batteries via a double iodine species fixation strategy with mesoporous carbon and modified separator. *J. Colloid Interface Sci.* **629**, 279–287 (2023). <https://doi.org/10.1016/j.jcis.2022.09.079>
42. L. Ma, Y. Ying, S. Chen, Z. Chen, H. Li et al., Electrocatalytic selenium redox reaction for high-mass-loading zinc-selenium batteries with improved kinetics and selenium utilization. *Adv. Energy Mater.* **12**(26), 2201322 (2022). <https://doi.org/10.1002/aenm.202201322>
43. L. Peng, Z. Wei, C. Wan, J. Li, Z. Chen et al., A fundamental look at electrocatalytic sulfur reduction reaction. *Nat. Catal.* **3**(9), 762–770 (2020). <https://doi.org/10.1038/s41929-020-0498-x>
44. Z.Q. Ye, Y. Jiang, L. Li, F. Wu, R.J. Chen, A high-efficiency cose electrocatalyst with hierarchical porous polyhedron nanoarchitecture for accelerating polysulfides conversion in Li-S batteries. *Adv. Mater.* **32**(32), 2002168 (2020). <https://doi.org/10.1002/adma.202002168>
45. X. Zhao, J. Yan, H. Hong, Y. Zhao, Q. Li et al., Ligand-substitution chemistry enabling wide-voltage aqueous hybrid electrolyte for ultrafast-charging batteries. *Adv. Energy Mater.* **12**(45), 2202478 (2022). <https://doi.org/10.1002/aenm.202202478>
46. X. Zhang, S. Wu, S. Deng, W. Wu, Y. Zeng et al., 3D CNTs networks enable MnO₂ cathodes with high capacity and superior rate capability for flexible rechargeable Zn–MnO₂ batteries. *Small Methods* **3**(12), 1900525 (2019). <https://doi.org/10.1002/smtd.201900525>
47. N. Zhang, Y. Dong, M. Jia, X. Bian, Y. Wang et al., Rechargeable aqueous Zn–V₂O₅ battery with high energy density and long cycle life. *ACS Energy Lett.* **3**(6), 1366–1372 (2018). <https://doi.org/10.1021/acscenergylett.8b00565>
48. X. Gao, Y. Zheng, J. Chang, H. Xu, Z. Hui et al., Universal strategy for preparing highly stable PBA/Ti₃C₂T_x mxene toward lithium-ion batteries via chemical transformation. *ACS Appl. Mater. Interfaces* **14**(13), 15298–15306 (2022). <https://doi.org/10.1021/acsaami.2c01382>

49. R. Venkatkarthick, N. Rodthongkum, X. Zhang, S. Wang, P. Pattanawat et al., Vanadium-based oxide on two-dimensional vanadium carbide mxene ($V_2O_x@V_2CT_x$) as cathode for rechargeable aqueous zinc-ion batteries. *ACS Appl. Energy Mater.* **3**(5), 4677–4689 (2020). <https://doi.org/10.1021/acsaem.0c00309>
50. Z. Yang, B. Wang, Y. Chen, W. Zhou, H. Li et al., Activating sulfur oxidation reaction via six-electron redox mesocrystal NiS_2 for sulfur-based aqueous batteries. *Natl. Sci. Rev.* (2022). <https://doi.org/10.1093/nsr/nwac268>
51. H. Li, M. Li, X. Zhou, T. Li, A novel rechargeable iodide ion battery with zinc and copper anodes. *J. Power Sour.* **449**, 227511 (2020). <https://doi.org/10.1016/j.jpowsour.2019.227511>
52. K. Lu, H. Zhang, F. Ye, W. Luo, H. Ma et al., Rechargeable potassium-ion batteries enabled by potassium-iodine conversion chemistry. *Energy Stor. Mater.* **16**, 1–5 (2019). <https://doi.org/10.1016/j.ensm.2018.04.018>
53. L. Yan, T. Liu, X. Zeng, L. Sun, X. Meng et al., Multifunctional porous carbon strategy assisting high-performance aqueous zinc-iodine battery. *Carbon* **187**, 145–152 (2022). <https://doi.org/10.1016/j.carbon.2021.11.007>
54. Y. Liu, J. Hu, Q. Lu, M. Hantusch, H. Zhang et al., Highly enhanced reversibility of a Zn anode by in-situ texturing. *Energy Stor. Mater.* **47**, 98–104 (2022). <https://doi.org/10.1016/j.ensm.2022.01.059>
55. Y. Zhang, L. Wang, Q. Li, B. Hu, J. Kang et al., Iodine promoted ultralow Zn nucleation overpotential and Zn-rich cathode for low-cost, fast-production and high-energy density anode-free Zn-iodine batteries. *Nano-Micro Lett.* **14**(1), 208 (2022). <https://doi.org/10.1007/s40820-022-00948-9>
56. Z. Qu, M. Zhu, Y. Yin, Y. Huang, H. Tang et al., A sub-square-millimeter microbattery with milliampere-hour-level footprint capacity. *Adv. Energy Mater.* **12**(28), 2200714 (2022). <https://doi.org/10.1002/aenm.202200714>
57. Z. Hou, T. Zhang, X. Liu, Z. Xu, J. Liu et al., A solid-to-solid metallic conversion electrochemistry toward 91% zinc utilization for sustainable aqueous batteries. *Sci. Adv.* **8**(41), eabp8960 (2022). <https://doi.org/10.1126/sciadv.abp8960>
58. M. Qiu, L. Ma, P. Sun, Z. Wang, G. Cui et al., Manipulating interfacial stability via absorption-competition mechanism for long-lifespan Zn anode. *Nano-Micro Lett.* **14**(1), 31 (2021). <https://doi.org/10.1007/s40820-021-00777-2>
59. L. Ma, X. Li, G. Zhang, Z. Huang, C. Han et al., Initiating a wearable solid-state Mg hybrid ion full battery with high voltage, high capacity and ultra-long lifespan in air. *Energy Stor. Mater.* **31**, 451–458 (2020). <https://doi.org/10.1016/j.ensm.2020.08.001>

